

Journal Pre-proof

Low cost Na₂FeSiO₄/H–N-doped hard carbon nanosphere hybrid cathodes for high energy and power sodium-ion supercapacitors

Honglu Wu, Yang Zhang, Xudong Zhang, Kwan San Hui, Jiefang Zhu, Wen He



PII: S0925-8388(20)32161-7

DOI: <https://doi.org/10.1016/j.jallcom.2020.155797>

Reference: JALCOM 155797

To appear in: *Journal of Alloys and Compounds*

Received Date: 22 January 2020

Revised Date: 23 May 2020

Accepted Date: 25 May 2020

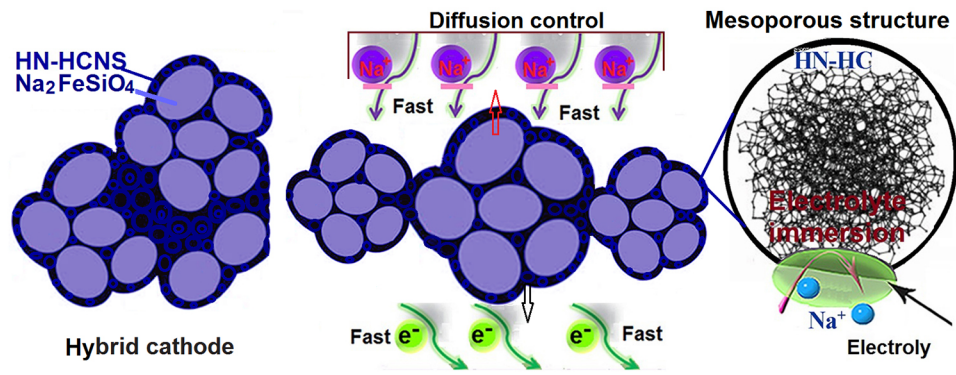
Please cite this article as: H. Wu, Y. Zhang, X. Zhang, K. San Hui, J. Zhu, W. He, Low cost Na₂FeSiO₄/H–N-doped hard carbon nanosphere hybrid cathodes for high energy and power sodium-ion supercapacitors, *Journal of Alloys and Compounds* (2020), doi: <https://doi.org/10.1016/j.jallcom.2020.155797>.

This is a PDF file of an article that has undergone enhancements after acceptance, such as the addition of a cover page and metadata, and formatting for readability, but it is not yet the definitive version of record. This version will undergo additional copyediting, typesetting and review before it is published in its final form, but we are providing this version to give early visibility of the article. Please note that, during the production process, errors may be discovered which could affect the content, and all legal disclaimers that apply to the journal pertain.

© 2020 Published by Elsevier B.V.

W.H.L.,X.D.Z. and W.H. conceived and designed the study. W.H.L. performed the experiments. W.H.L.and Y.Z. wrote the paper. All authors reviewed and edited the manuscript. And All authors read and approved the manuscript.

Journal Pre-proof



Journal Pre-proof

Low cost $\text{Na}_2\text{FeSiO}_4/\text{H-N-doped}$ hard carbon nanosphere hybrid cathodes for high energy and power sodium-ion supercapacitors

Honglu Wu^a, Yang Zhang^b, Xudong Zhang^{a,*}, Kwan San Hui^c, Jiefang Zhu^d, and Wen He^{a,*}

^aCollege of Material Science and Engineering, Qilu University of Technology (Shandong Academy of Sciences), Jinan 250353, China

^bCollege of Automation, Beijing Information Science and Technology University, Beijing, 100192, China

^cEnergy and Environment Laboratory, School of Engineering, University of East Anglia (UEA), Norwich, NR4 7TJ, United Kingdom.

^dDepartment of Chemistry-Ångström Laboratory, Uppsala University, Box 538, SE-75121 Uppsala, Sweden.

*Corresponding author. Tel. +86 18353108836, E-mail address: hewen1960@126.com (W. He), <https://scholar.google.com/citations?user=pBdTfOUAAAAJ&hl=en>.

Abstract

$\text{Na}_2\text{FeSiO}_4$ (NFS)/H-N-doped hard carbon nanospheres (HN-HCNSs) hybrid cathodes have been synthesized by using ferrous gluconate as template and carbon source via sol-gel method for the first time. In the structure of this hybrid cathode, the ultrathin NFS nanosheets are uniformly anchored in the mesoporous network structure of HN-HCNSs coating, forming the fast conductive transport pathways for electrons and Na^+ -ions. The NFS/HN-HCNSs hybrid cathode shows a hybrid energy storage mechanism with high initial discharge capacity of 218.4 mAh g^{-1} at 0.1 C and in the voltage

range of 1.2–4.6 V versus Na/Na⁺. It also shows excellent long-term cycling stability (the capacity retention rates of 73.8% at 1 C after the 3300 cycles and 56.8% at 5 C after the 750 cycles in the voltage range of 1.5–4.6 V). Moreover, the unique mesoporous carbon-coated structural features endow the hybrid cathode with a maximum energy density of 331.99 W h kg⁻¹ and a maximum power density of 2431.87 W kg⁻¹ within working voltage range of 1.5–4.6 V.

Keywords: hybrid cathode; Na₂FeSiO₄; H-N-doped hard carbon nanosphere; mesoporous carbon-coated structure; ferrous gluconate

1. Introduction

Low cost lithium ion batteries (LIBs) with high energy/power densities, high rate performance and long cycling stability have attracted enormous attention due to good safety and its potential applications in future electric vehicles, smart electric grids, and even miniaturized electronic/optoelectronic devices, etc [1-4]. In design and fabrication of low-cost sodium ion batteries (SIBs), the rational design of promising cathode is highly challenging yet critically important in practical applications. However, lithium resource storage is limited and expensive, while sodium ion storage is abundant and performance is similar to lithium, so low-cost SIBs have become potential alternatives to LIBs and are widely welcomed. After the advent of SIBs, various cathode materials, such as layered transition-metal oxides, NaFePO₄, and Na₃V₂(PO₄)₃ and so on have been investigated extensively [5-7]. However, metal oxides present relatively low operating potentials (ca. 2.8 V) and a poor cycling stability due to larger expansion. Phosphate cathode materials contribute lower capacities owing to poor reaction kinetics or a large molecular weight [8]. Owing to the large ionic radius of the Na⁺, cathode materials have to bear complicated electrochemical behaviors and larger structure evolution during reversible charge and discharge, leading to severe capacity fading with extended cycling. Therefore, cathode materials with low cost,

safety and high cycling stability should be developed for high energy/power SIBs.

Among cathode materials, sodium iron silicate ($\text{Na}_2\text{FeSiO}_4$) (NFS) was regarded as one of the most promising cathode materials for low cost SIBs due to the cheap and abundant resources of Na, Fe and Si, low toxicity, safety characteristics, robustly crystal structure and high specific capacity [9-12]. Zhao et al. firstly explored the possible structures of NFS by the first principles calculations [13]. They found that the crystal structure of NFS is similar to $\text{Li}_2\text{FeSiO}_4$, inclining to three-dimensional Fe–Si–O framework composed of interconnected tetrahedrons of SiO_4 , FeO_4 and NaO_4 [14]. In theory, NFS has a high theoretical capacity of 276 mAh g^{-1} through two-electron reactions [12,15]. However, the inherent low electron conductivity and slow sodium ion diffusion of Fe–Si–O framework limit its application in high power SIBs [11,16]. In order to improve electron/ion transport kinetics of the NFS, several approaches have been attempted, such as the addition of various carbon (e.g., carbon nanotube [15,16], citric acid [10] and sucrose [12], etc.), nanocrystallization and porous structure of NFS [17]. Guan et al.[12] prepared a NFS/C composite with three-dimensional network morphology by using sucrose as carbon source, which has a relatively pure triclinic phase and exhibits the highest reversible specific capacity of 181 mAh g^{-1} at C/10 ($1 \text{ C} = 276 \text{ mA g}^{-1}$) and 88% capacity retention after 100 cycles in the voltage range of 1.5-4.5 V. To improved electronic conductivity, NFS/C composites with cubic structure and different morphology, such as nanocrystals [15], irregular sphere-like particles [18], interconnected mesoporous NFS nanospheres supported on carbon nanotubes [16] have been successfully synthesized through different routes. However, they all have a poor cycle performance (Support information Table S1). At present, NFS with high energy and power densities as well as long cycling life has rarely been realized and reported.

Ferrous gluconate as a template and carbon source has aroused considerable interests in synthesis of energy storage materials because of its unique properties and multiple functional groups [19,20]. Herein, we develop low cost sodium-ion supercapacitors (SISs) with high energy/power densities by using $\text{Na}_2\text{FeSiO}_4$ (NFS)/H-N-doped hard carbon nanosphere (HN-HCNS) hybrid cathode. The NFS/HN-HCNS hybrid cathode with mesoporous carbon-coated structure and mesoporous structure was synthesized by using ferrous gluconate as a template and carbon source via sol-gel method for the first time. The synthesis conditions (such as additive amount of ferrous gluconate, annealing temperature and holding time) were optimized, and the synthesis mechanism was proposed. The challenge of this design is to retain efficient Na ion diffusion in NFS/HN-HCNS hybrid cathode due to its unique structure. The NFS/HN-HCNS hybrid cathode can achieve high energy and power densities as well as long cycling life for SISs. Several merits of this design have: (1) H-N-doped hard carbon nanospheres (about 7.98 wt.%) provide high electron conductivity and more Na ion storage sites; (2) mesoporous structure makes the Na ions and electrolyte easily penetrate; (3) unique mesoporous carbon-coated structure has high interface areas for the insertion/extraction of Na ions and fast Na^+ migration, which is the most significant factor for high rate performance and excellent long cycling life; (4) H-N-doping (H:1.07 wt.%, N:0.55 wt.%) in HN-HCNS can adjust the surface functional groups of carbon, enhancing electric conductivity, in favor of the charge transfer and electrode–electrolyte interactions [21-23]; (5) the ferrous gluconate is based on abundant renewable resource, which makes this synthesis technology simple and cost effective. Owing to these merits, the NFS/HN-HCNS hybrid cathode exhibits the high energy and power densities as well as long cycling life, which are among the best thus far reported for NFS (Table S1 lists some recently reported NFS).

2. Experimental

2.1. Materials synthesis

Anhydrous sodium acetate (CH_3COONa), tetraethyl orthosilicate (TEOS) and ammonia ($\text{NH}_3\cdot\text{H}_2\text{O}$) were purchased from Damao Chemical Reagent Factory. Ferrous gluconate ($\text{C}_{12}\text{H}_{22}\text{FeO}_{14}\cdot 2\text{H}_2\text{O}$) was obtained from Shanghai Macklin Biochemical Co., Ltd. And iron nitrate nonahydrate ($\text{Fe}(\text{NO}_3)_3\cdot 9\text{H}_2\text{O}$) was from Tianjin Hengxing chemical reagent Co., Ltd. Preparation of $\text{Na}_2\text{FeSiO}_4$ (NFS) precursors by sol-gel method and the specific synthetic route is shown in Fig. S1. Typically, stoichiometric amounts of tetraethyl orthosilicate (TEOS) were dissolved in deionized water and ethanol under stirring at 45 °C. And a certain amount of nitric acid is added for catalysis. Then, stoichiometric CH_3COONa (AR) was dispersed in deionized water and added into this solution under continuous stirring. Meanwhile, a certain molar ratio of $\text{Fe}(\text{NO}_3)_3\cdot 9\text{H}_2\text{O}$ (AR) and $\text{C}_{12}\text{H}_{22}\text{FeO}_{14}\cdot 2\text{H}_2\text{O}$ (AR) were added to the solution and use ammonia to adjust the pH to 4-5 while stirring for 4 h. The solution was allowed to stand for 3 days to form a sol at room temperature. After being dried at 60 °C all day, the dry gel was ground to powders. Lastly, the resultant powder was heated at 300 °C for 3 h. The precursor further calcined at different temperature 650 °C in a tubular furnace under N_2 atmosphere over 8 h with a ramping rate of 3 °C min^{-1} . The precursors of $\text{Fe}(\text{NO}_3)_3\cdot 9\text{H}_2\text{O}$ and $\text{C}_{12}\text{H}_{22}\text{FeO}_{14}\cdot 2\text{H}_2\text{O}$ with a molar ratio of 4:6, 3:7, 2:8 and 1:9 are labeled as NFS/HN-HCNS-1, NFS/HN-HCNS-2, NFS/HN-HCNS-3 and NFS/HN-HCNS-4, respectively.

2.2. Characterization

The composite samples were characterized by powder X-ray diffraction (XRD, Shimadzu-6100, $\text{CuK}\alpha$ radiation, in the range of 2θ angles of 10 ° to 70 °), transmission electron microscopy (TEM, Talos F2100X) and Raman (LabRam HR). The morphology of the sample was observed by a

scanning electron microscope (SEM, ZEISS SUPRA 40). The pore size distribution and nitrogen adsorption-distribution isotherm were measured at 77 K on an adsorption analyzer (Micromeritics, Gemini V2380, USA) to analyze specific surface area and pore size distribution.

2.3 Electrochemical evaluation

The working electrode was mixed with a NFS/HN-HCNS active material (70 wt.%), a polyvinylidene fluoride (PVDF) binder (10 wt.%) and acetylene black (20 wt.%) in a solvent of N-methylpyrrolidone (NMP), and then coated on an aluminum foil. Subsequently, after drying at 110 °C overnight in a vacuum drying oven, the NFS/HN-HCNS cathode was made into a wafer with an area of 1.76 cm², which the average load was about 1.0 mg/cm².

Using a sodium metal as a reference electrode, a Whatmanglass microfiber filter (GF/F grade) was used as a polypropylene separator, and a CR 2032 coin cell was assembled in a glove box (MBraun, Germany) filled with a high purity argon atmosphere (O₂ and H₂O levels < 0.01pp). A 1 M NaClO₄ solution in EC: PC (1:1) +5% FEC was used as the electrolyte. The galvanostatic cycle stability and rate performance (relative to Na⁺/Na) of the battery was tested on a Channels battery analyzer (CT3008W) with a voltage range of 1.5-4.6 V. The cyclic voltammetry (CV) voltage range of 1.4-4.6 V was tested on a PARSTAT 2263 electrochemical workstation. Electrochemical impedance spectroscopy (EIS) studies were performed on a Solartron Analytical instrument in the frequency range of 0.01 Hz to 100 kHz.

3. Results and discussion

The NFS/HN-HCNSs hybrid cathodes were synthesized by using ferrous gluconate as a template and carbon source via sol-gel method. Ferrous gluconate controlled the formation of nanocomposite structure and enhanced electrochemical performances of the NFS/HN-HCNSs hybrid

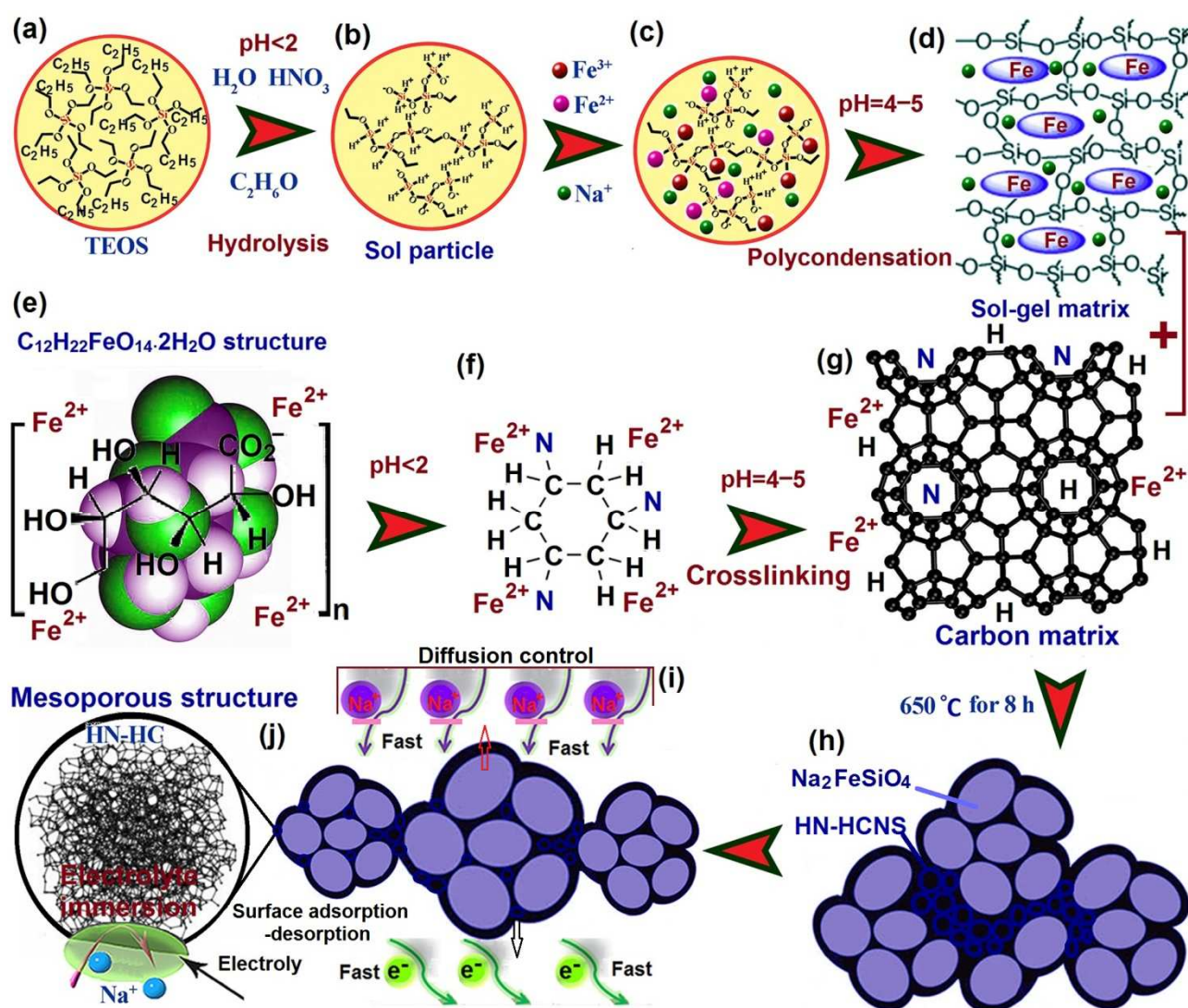


Fig. 1. (a-d) Schematic diagram of sol-gel process, (a,b) TEOS hydrolysis process, (c) self-assembly of sol particle with metal ions, (d) structure of sol-gel matrix. (e-g) Schematic presentation of crosslinking and carbonizing process of ferrous gluconate, (e) structure of ferrous gluconate, (f, g) crosslinking reaction of ferrous gluconate. (h) Structure model of NFS/HN-HCNSs. (i, j) Schematic diagram of the Na^+ rapid diffusion during charge and discharge.

cathodes. The formation mechanism of NFS/HN-HCNS was illustrated in Fig. 1. To obtain a smaller sol particle size, nitric acid was used as catalyst for adjusting hydrolysis reaction of TEOS solution (Fig. 1ab). When Fe cations were added into the sol solution, they were combined with the sol particles (Fig. 1c), and were self-assembled to the surface of sol particles by electrostatic interaction. To obtain sol-gel matrix, the nitric acid was used as catalyst for adjusting polycondensation reaction of sol solution (Fig. 1d). Ferrous gluconate was naturally crosslinked through the nitric acid

oxidation (Fig. 1ef) and carbon matrix was formed by adding ammonium hydroxide to adjust the pH value in the sol-gel process (Fig. 1g). Finally, sol-gel matrix particles assembled with carbon matrix particles at high temperature and formed NFS/HN-HCNSs hybrid cathode (Fig. 1h). The unique carbon-coated structure has high interface areas for the insertion/extraction of Na ions and fast electron and Na⁺ migration (Fig. 1i), and mesoporous structure in HN-HCNS-coated layer makes the Na ions and electrolyte easily penetrate (Fig. 1j).

The crystal structure of Na₂FeSiO₄ has the complex families of the robust Fe–Si networks and only two phases (triclinic cell and cubic cell) have been synthesized at present [10,12,24]. The XRD patterns of the of different samples synthesized with different molar ratio of Fe(NO₃)₃·9H₂O and C₁₂H₂₂FeO₁₄·2H₂O at 650 °C for 8 h are shown in Fig.2a. The main diffraction peaks in each sample can be well matched with the cubic crystal system structure of Na₂FeSiO₄ with a space group of Fm-3m, which is isostructural to Na₂CaSiO₄ (PDF#01-1067) [10,25]. Apparently, all the sample have sharp and intense (111) diffraction peak, showing the well-crystallized characteristics.

Summary of the structural features of the different samples calculated by using Jade 6 XRD pattern-processing software is shown in Table S2. By comparison, it can be found that the (222) diffraction peak intensity of NFS/HN-HCNS-3 is higher than that of other samples. NFS/HN-HCNS-3 has larger cell volume and smaller strain, indicating that the crystal growth of NFS can be controlled by ferrous gluconate. The element contents of the different samples synthesized with different molar ratio of Fe(NO₃)₃·9H₂O and C₁₂H₂₂FeO₁₄·2H₂O at 650 °C for 8 h were determined by using Vario EL III CHN elemental analyzer (Table S3). The results show that the carbon content increases as the molar ratio of Fe(NO₃)₃·9H₂O and C₁₂H₂₂FeO₁₄·2H₂O increases. The NFS/HN-HCNS-3 has carbon content of 7.98 wt%, hydrogen content of 1.07 wt% and nitrogen

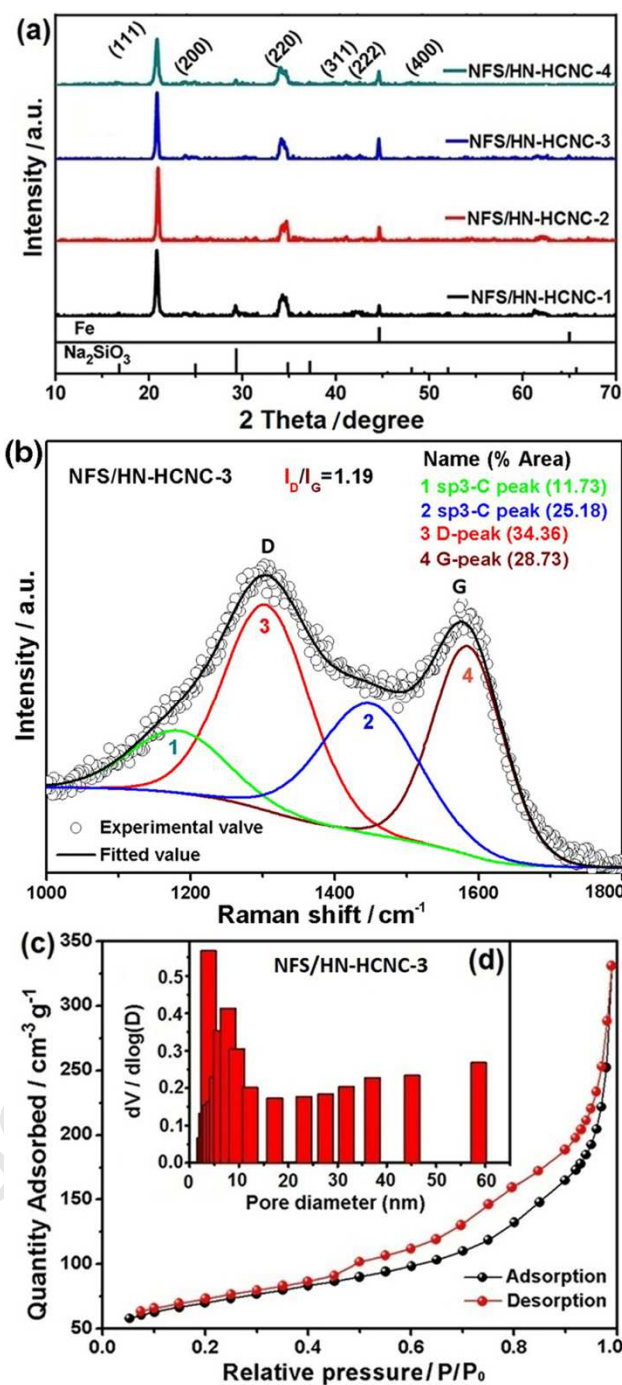


Fig.2. (a) XRD patterns of different samples synthesized with different molar ratio of $\text{Fe}(\text{NO}_3)_3 \cdot 9\text{H}_2\text{O}$ and $\text{C}_{12}\text{H}_{22}\text{FeO}_{14} \cdot 2\text{H}_2\text{O}$ at 650°C for 8 h, NFS/HN-HCNS-1 (4:6), NFS/HN-HCNS-2 (3:7), NFS/HN-HCNS-3 (2:8) and NFS/HN-HCNS-4 (1:9). (b) Raman spectrograms deconvoluted by four Gaussian peaks for NFS/HN-HCNS-3 sample. (c) Nitrogen adsorption-desorption isotherm of NFS/HN-HCNS-3, the insert (d) is Barret-Joyner-Halenda (BJH) pore size distribution curve of NFS/HN-HCNS-3.

content of 0.55 wt%, but no diffraction peaks of graphitized carbon are detected from the X-ray diffraction pattern in Fig. 2a, suggesting that the carbon in NFS/HN-HCNS-3 belongs to the

amorphous structure [26,27]. As the carbon content increases, the intensity of (111) peak decreases and the peak width increases, indicating that the carbon in the sample inhibited the crystal growth of NFS [28,29].

In order to further analyze the composition and structure of carbon layers, Raman spectra of the NFS/HN-HCNS-3 are shown in Fig.2b. It can be clearly seen that the two characteristic bands located at 1308 cm^{-1} and 1585 cm^{-1} are D-band (disordered carbon) and G-band (graphitized carbon), respectively. The two broad peaks of the NFS/HN-HCNS-3 can be deconvoluted into four peaks (Peak 1, Peak 2, Peak 3, and Peak 4) using Gaussian numerical simulation, which are attributed to four vibration modes of the coated carbon [27,30]. The bands near 1178 cm^{-1} (peak 1) and 1446 cm^{-1} (peak 2) are related to sp^3 type carbon (amorphous carbon and the defects), while 1308 cm^{-1} (peak 3) and 1585 cm^{-1} (peak 4) is sp^2 type carbon (graphitized carbon). According to the peak area, the peak intensity ratio (I_D/I_G) of the D-band and G-band for NFS/HN-HCNS-3 is 1.19, indicating that the fraction of graphitized carbon is not high, and the residual carbon in NFS/HN-HCNS-3 is mainly hard carbon [26]. The presence of hard carbon not only inhibits the growth and aggregation of NFS nanoparticles during synthesis process, but also improves the electronic conductivity of the hybrid electrode and ensures the fast transport of sodium ions [31].

To examine the mesoporous structure, Fig 2c shows the N_2 adsorption/desorption isotherm of NFS/HN-HCNS-3 sample. According to the International Union of Pure and Applied Chemistry (IUPAC) regulation [32], the NFS/HN-HCNS-3 sample has a typical type IV isotherm and H3-type hysteresis loop caused by non-uniform wormlike pores, indicating typical mesoporous characteristics [33,34]. Its BJH pore-size-distribution shows a wide pore size distribution of 2–48 nm (Fig. 2d), which was also observed with HRTEM image (Fig. 4f). The NFS/HN-HCNS-3 has higher specific

surface areas of $143 \text{ m}^2 \text{ g}^{-1}$ and larger pore volume of 0.45 cc/g , increasing the contact area between the cathode and the electrolyte. These mesopores are mainly contributed from the interstices among the assembled nanoparticles and generated by the decomposition of ferrous gluconate in the calcination process. Due to the presence of mesopores, NFS/HN-HCNS-3 can significantly increase the permeability of the electrolyte, which makes Na ions in electrolyte easily react with NFS nanosheets.

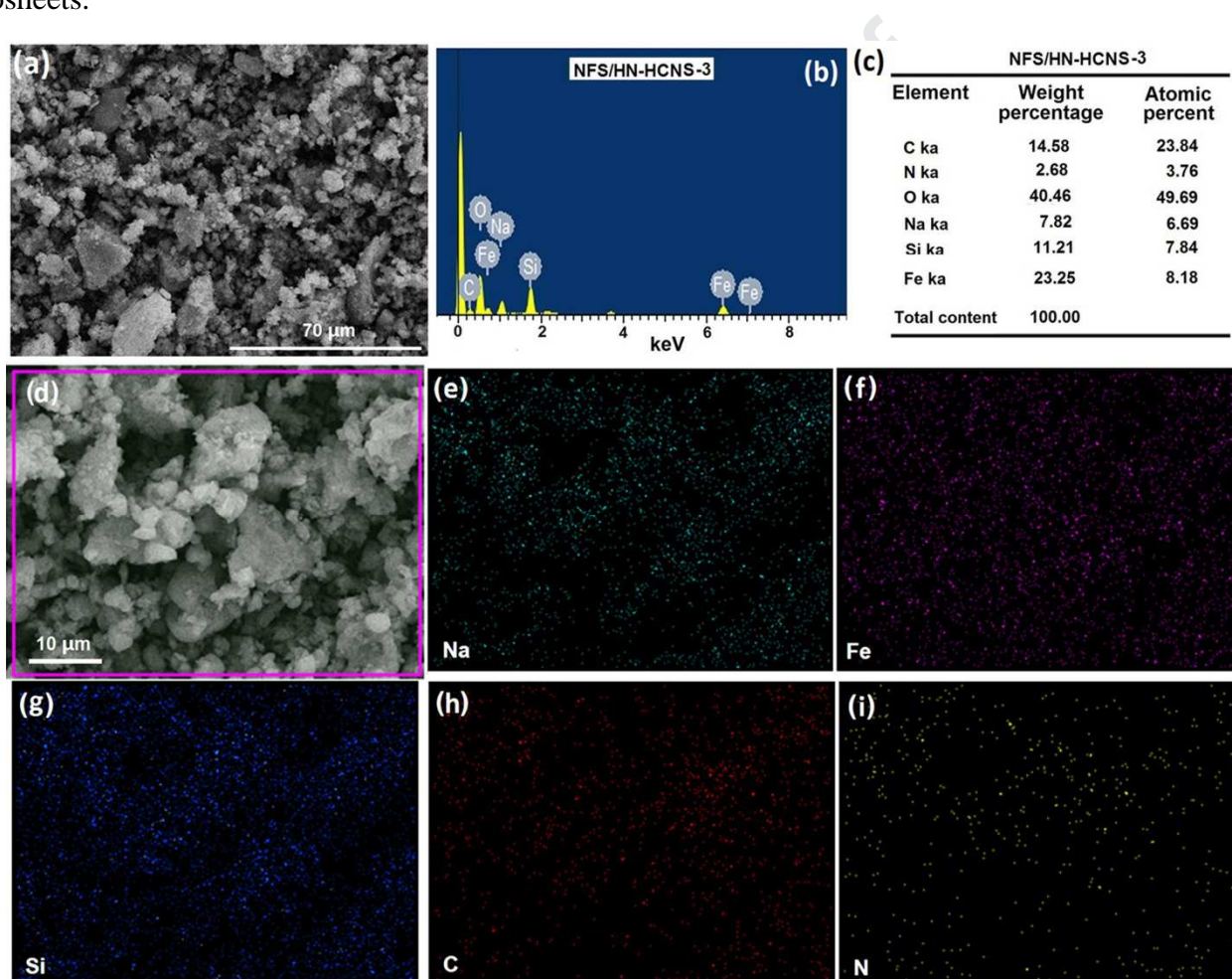


Fig. 3. (a) SEM image of NFS/HN-HCNS-3. (b) SEM-EDS spectrum and (c) element contents in NFS/HN-HCNS-3. (d) typical SEM image of NFS/HN-HCNS-3 sample and the corresponding elemental mappings of sodium (e), iron (f), silicon (g), carbon (h), nitrogen(i).

To further characterize the components of NFS/HN-HCNS-3 sample, scanning electron microscopy (SEM) and X-ray energy dispersive spectrometry (EDS) quantitative analysis have been performed (Fig. 3). Fig. 3a shows a SEM image of NFS/HN-HCNS-3 in the larger sweep area and

Fig. 3b is a SEM-EDS spectrum in the corresponding sweep area, displaying the EDS spectra of different elements in Fig. 3a and indicating that the NFS/HN-HCNS-3 contains Na, O, Fe, Si, N and C elements. The computed contents of different elements in the micrometer range are showed in Fig. 3c. The results show that the carbon content (14.58 wt%) and nitrogen content (2.68 wt%) of NFS/HN-HCNS-3 are higher than these determined by using Vario EL III CHN elemental analyzer (Table S3) because the HN-HCNS was coated on the surface of NFS nanosheets. Fig. 3d is a SEM image of NFS/HN-HCNS-3 sample in the smaller sweep area and Fig. 3e–i show the elemental mapping images of Fe, Na, Si, C and N in the NFS/HN-HCNS-3 sample, which confirm further the existence and uniform distribution of elements, the carbon-coating and nitrogen-doping.

The morphology and fine microstructure of NFS/HN-HCNS-3 are characterized by FESEM and HRTEM (Fig. 4). SEM images of different electrodes are shown in Fig. S2. It can be clearly see that the different samples have different particle size and morphologies, which shows that the ferrous gluconate template can effectively control the formation of NFS/HN-HCNS. The NFS/HN-HCNS-3 sample has a more uniform particle size distribution and has a higher electrical conductivity compared to other samples. The SEM image in Fig. 4a shows a large carbon decorated sheet that it is composed of 200-500nm primary particles (Fig. 4d) aggregated together to form secondary particle. The enlarged SEM image (Fig. 4b) indicates the existence of many white HN-HC nanospheres with the size of 10–20 nm on the surface of this sheet, which is consistent with the result of HRTEM image in Fig. 4e, showing the disordered nanostructure of HN-HC nanospheres.

TEM image in Fig. 4c shows a primary particle with mesoporous carbon-coated structure, which is composed of HN-HC nanospheres and NFS nanosheets (Fig.4d). HRTEM image in Fig. 4e shows that the HN-HC-coated layer is consist of the disordered nanospheres of different sizes and

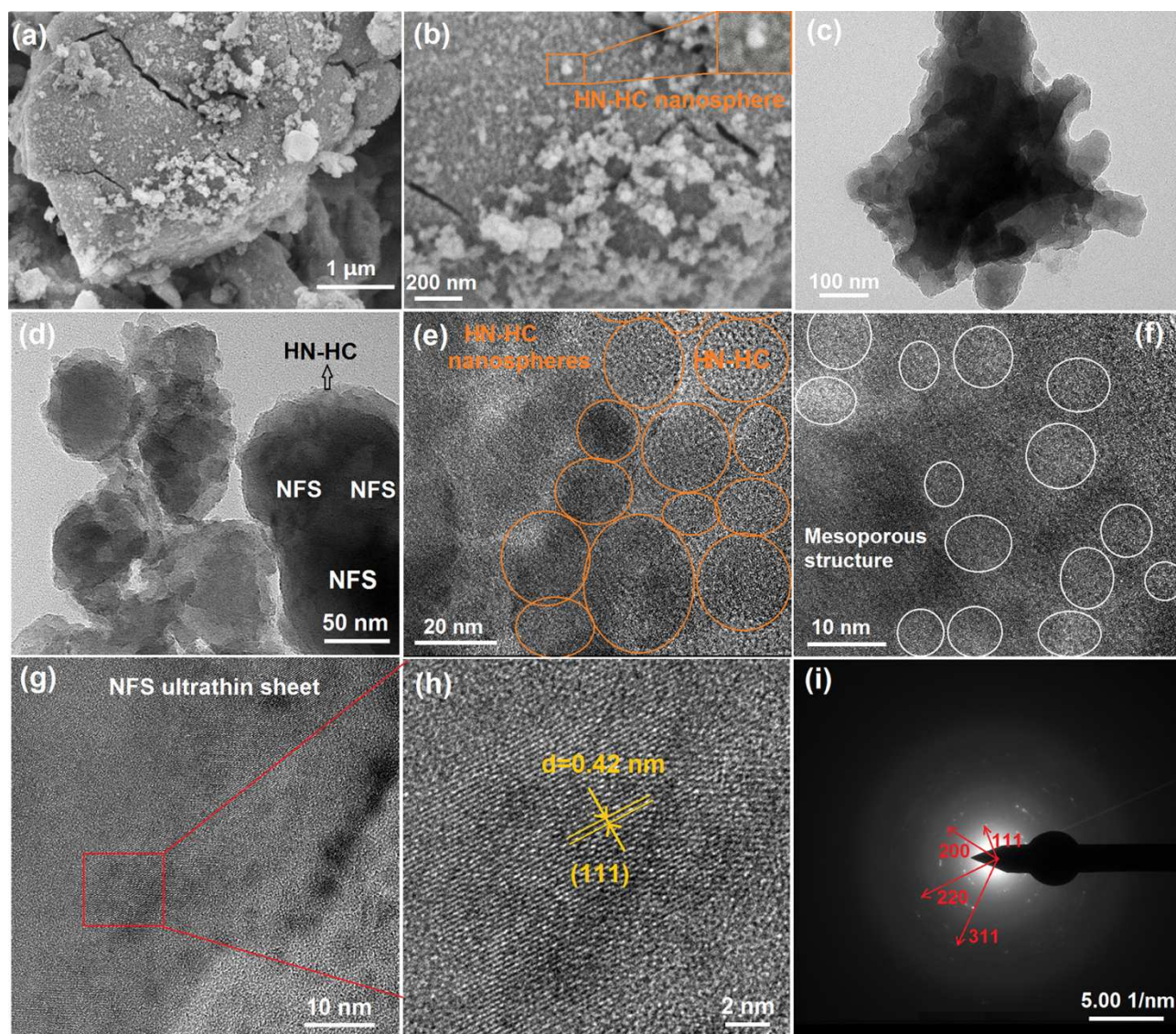


Fig. 4. (a, b) SEM images of NFS/HN-HCNS-3 sample. (c, d) TEM images of NFS/HN-HCNS-3 electrode with N-HC layer. (e-g) HRTEM images of NFS/HN-HCNS-3 sample. (h) Lattice fringe image of NFS/HN-HCNS-3 sample. (i) Electron diffraction image of NFS/HN-HCNS-3 sample.

Fig. 4f shows the mesoporous network structure in HN-HC coating, The HN-HC-coated layer on the surface of NFS is converted from ferrous glucose and connects the NFS nanosheets to form NFS/HN-HCNSs nanocomposites. Fig. 4gh clearly display a ultrathin NFS nanosheet and its lattice fringes of 0.42 nm corresponding to (111) crystal plane of the space group Fm-3m, respectively. The electron diffraction image (Fig. 4i) of NFS/HN-HCNS-3 sample shows the electron diffraction concentric rings of different crystal planes, which indicates that NFS is also composed of

nanocrystalline particles. The results of SEM and HRTEM further proved that the synthesis mechanism proposed in Fig. 1 is reasonable.

In order to optimize the synthesis, Na ion half-cells were assembled with the different NFS/HN-HCNS hybrid electrodes with the average load of about 1.0 mg/cm^2 as cathodes, Na metal as the counter electrode, and 1 M solution of NaClO_4 in EC: PC (1:1) +5% FEC as the electrolyte. The electrochemical properties of the different electrodes were evaluated in the voltage range of 1.5-4.6 V versus Na/Na^+ . Fig. 5 and Fig. S3 show that the electrochemical performances of the different NFS/HN-HCNS hybrid electrodes synthesized under the different preparation conditions, respectively. The results indicate that the NFS/HN-HCNS-3 hybrid electrode synthesized at 650°C for 8 h has a initial discapacity of 146.1 mAh g^{-1} (Fig. S3a) at a current density of 0.1 C (1 C = 276 mAh g^{-1}), the best rate performance (Fig. 5ad), the smallest charge transfer resistance ($R_{\text{ct}}=144.24 \Omega$) (Fig. 5be and Tables S4 and S5), the fastest sodium ion diffusion coefficient ($D_{\text{Na}^+}=1.81 \times 10^{-14} \text{ cm}^2 \text{ s}^{-1}$) (Fig. 5cf and Tables S4 and S5), and the best energy/power performance ($331.99 \text{ W h kg}^{-1}/50.45 \text{ W kg}^{-1}$ and $68.49 \text{ W h kg}^{-1}/2431.87 \text{ W kg}^{-1}$) (Fig. S3cf and Table S7).

The NFS/HN-HCNS-3 hybrid electrode not only exhibits and the stable charge/discharge capacity profiles for different cycles at 0.2 C (Fig. S5a) and the stable cyclic voltammetry (CV) curves for different cycles at the sweep rate of 2.5 mV s^{-1} (Fig. S5b), but also delivers a ultra-long cycling ability (initial capacity of 65.6 mAh g^{-1} and the capacity retention rate of 73.8% after 3300 cycles) at 1 C (Fig. 5g), which is the longest cycling ability among all reported NFS cathodes previously (Table S1). During the cycle, its discharge capacity increases first and then decreases because the internal active material in the NFS/HN-HCNS-3 hybrid electrode is gradually activated with an increase in the number of charge and discharge times, resulting in an increase in capacity.

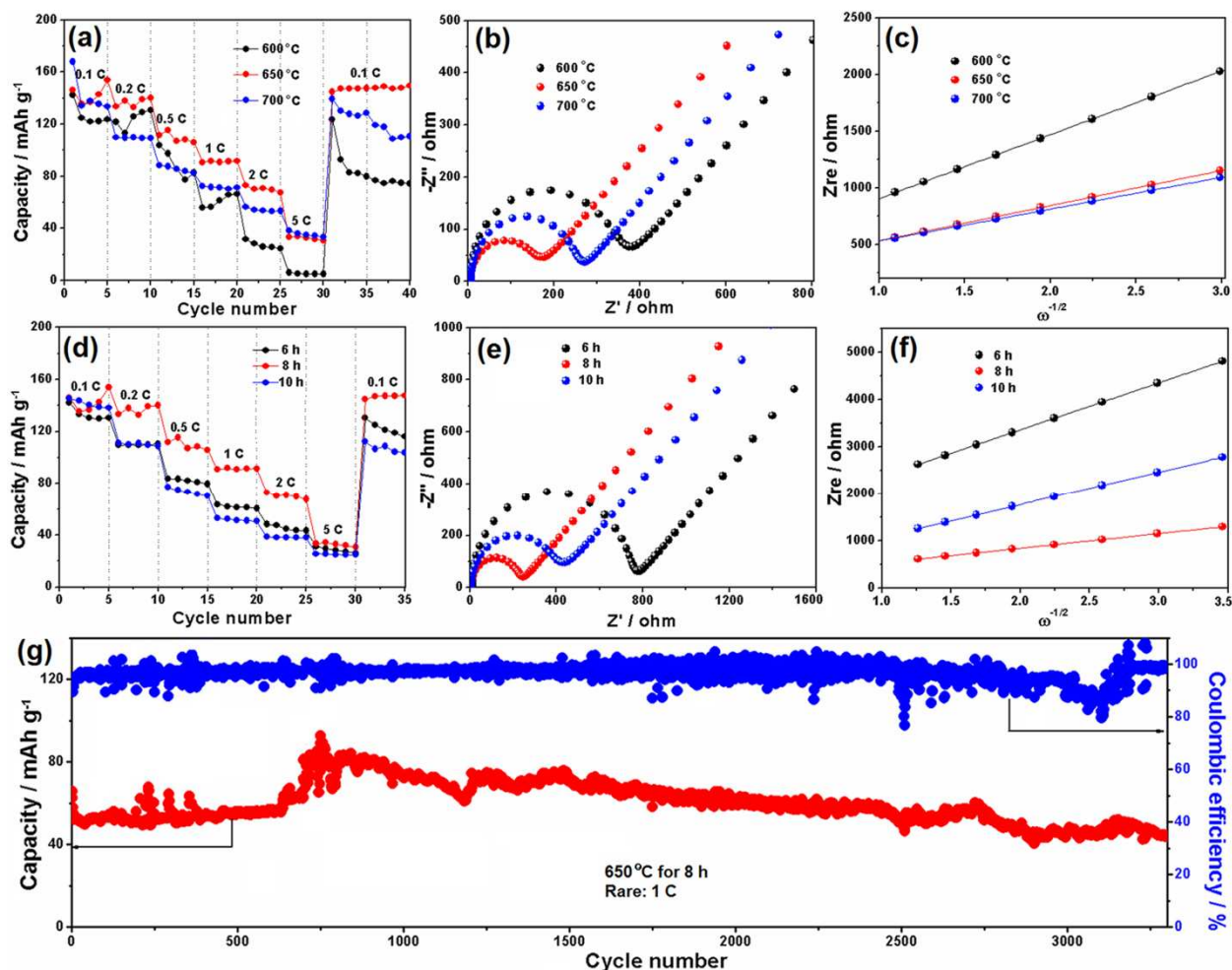


Fig. 5. (a) Rate performances, (b) EIS curves and (c) the relationship between the slope of the plot of Z_{re} and the reciprocal root square of frequency ($\omega^{-1/2}$) at low frequencies in (b) for the different electrodes synthesized at different annealing temperatures for 8 h, EIS curves were tested in the frequency range of 0.01-10⁵ Hz at the completely uncharged/undischarged state. (d) Rate performances, (e) EIS curves and (f) the relationship between Z_{re} and $\omega^{-1/2}$ at low frequencies in (e) for the different electrodes synthesized at 650 °C for different holding time. (g) Long-term cycling stability of NFS/HN-HCNS-3 electrode synthesized at 650 °C for 8 h for 3300 cycles at 1C in the voltage range of 1.5-4.6 V.

Later, as the number of cycles increased, the deactivation of some active substances deteriorated, resulting in a gradual decline in capacity. Besides, the electrolyte decomposition at a relatively high potential (4.5 V) might also be responsible for the capacity fading on subsequent cycles [35,36]. The capacity retention rate of the NFS/HN-HCNS-3 hybrid electrode after 700 cycles was maintained at 600 °C and 700 °C for 8 h (Fig. S5d), only 12.9% and 9.2% at 1 C.

Fig. 6, Fig. S4 and S6 show the electrochemical performances of the different electrodes

synthesized with different molar ratio of $\text{Fe}(\text{NO}_3)_3 \cdot 9\text{H}_2\text{O}$ and $\text{C}_{12}\text{H}_{22}\text{FeO}_{14} \cdot 2\text{H}_2\text{O}$ at $650\text{ }^\circ\text{C}$ for 8 h. The results indicate that the NFS/HN-HCNS-3 hybrid electrode synthesized with the molar ratio of 2:8 at $650\text{ }^\circ\text{C}$ for 8 h has higher discharge capacity of 138.1 mAh g^{-1} for second cycle at 0.1 C (Fig. 6a), the best rate performance (Fig. 6b and Fig. S4c), the smallest charge transfer resistance ($R_{\text{ct}}=144.24\ \Omega$) (Fig. 6e and Tables S6), the fastest sodium ion diffusion coefficient ($D_{\text{Na}^+}=1.81 \times 10^{-14}\text{ cm}^2\text{ s}^{-1}$) (Fig. 6f and Tables S6), and the best energy/power performance ($331.99\text{ W h kg}^{-1}/50.45\text{ W kg}^{-1}$ and $68.49\text{ W h kg}^{-1}/2431.87\text{ W kg}^{-1}$) (Fig. 6c and Table S7). The morphology of CV curves of the different electrodes synthesized with different molar ratio in Fig. 6d has little change as the increase of molar ratio of $\text{Fe}(\text{NO}_3)_3 \cdot 9\text{H}_2\text{O}$ and $\text{C}_{12}\text{H}_{22}\text{FeO}_{14} \cdot 2\text{H}_2\text{O}$, showing that the carbon content only affected the electrical conductivity of electrodes and did not influenced the redox reaction of $\text{Na}_2\text{FeSiO}_4$. Fig. S6a presents the typical charge/discharge profiles of of the different electrodes at 0.1 C . Apparently, two charge/discharge voltage plateaus are observed at around $4.65\text{ V}/1.65\text{ V}$ during the initial charge process for NFS/HN-HCNS-3 (Fig. S6b), which could be assigned to the single electron electrochemical reaction corresponding to the $\text{Fe}^{2+}/\text{Fe}^{3+}$ and $\text{Fe}^{3+}/\text{Fe}^{4+}$ redox reaction [12,14]. Compared to other electrodes, NFS/HN-HCNS-3 shows a better reversibility and a initial capacity of 146.1 mAh g^{-1} corresponding to 1.05 mol of Na ion in the structure of NFS/HN-HCNS-3. Moreover, the second charge and discharge capacity (Fig. S6b) is lower than the initial charge and discharge capacity (Fig. S6a). The reasons of capacity fading may be the irreversible reduction of electrode caused by structural rearrangement [27,29] and the

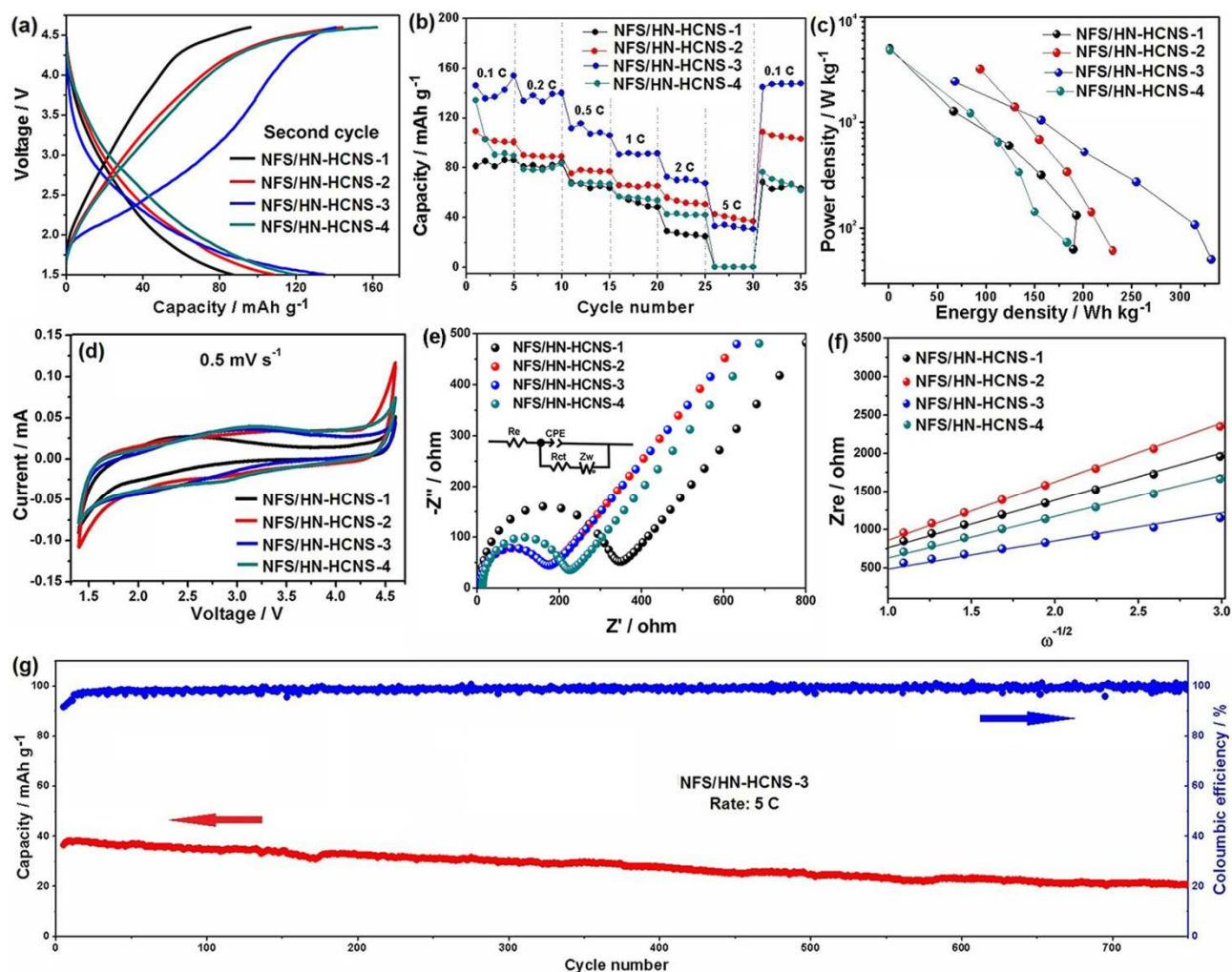


Fig. 6. Electrochemical performances of different electrodes synthesized with different molar ratio of $\text{Fe}(\text{NO}_3)_3 \cdot 9\text{H}_2\text{O}$ and $\text{C}_{12}\text{H}_{22}\text{FeO}_{14} \cdot 2\text{H}_2\text{O}$ at 650°C for 8 h, NFS/HN-HCNS-1 (4:6), NFS/HN-HCNS-2 (3:7), NFS/HN-HCNS-3 (2:8) and NFS/HN-HCNS-4 (1:9). (a) The second charge and discharge profiles at 0.1C; (b) Rate performance at various current densities; (c) A comparison of the energy and power performance; (d) CV curves at 0.5 mV s^{-1} vs Na/Na^+ in the voltage range of 1.4–4.6 V; (e) EIS curves based on the fitted equivalent circuit; (f) the relationship between Z_{re} and $\omega^{-1/2}$ at low frequencies; (g) Long-term cycling stability of the NFS/HN-HCNS-3 electrode at 5C in the voltage range of 1.5–4.6 V.

formation of SEI layer on the surface of electrode [37,38]. The SEI layer can prevent structural collapse and increase the cycle life of the electrode material, but it consumes a part of sodium ions and generates the irreversible capacity during the formation process. This demonstrates the possibility for developing high energy and power densities as well as long cycling life cathodes by single electron electrochemical reaction in the unique structure. Additionally, Fig S7 shows the electrochemical data of NFS/HN-HCNS-3 electrode in the voltage range of 1.2–4.6 V. Among them,

the first discharge and charge specific capacities of the initial cycle are 218.4 mAh g⁻¹ and 165.0 mAh g⁻¹ at 0.1 C (Fig S7a), respectively. Compared with the specific capacity (146.1 mAh g⁻¹) in the voltage range of 1.5–4.6 V (Fig S5a), the first discharge capacity of NFS/HN-HCNS-3 electrode has increased by 72.3 mAh g⁻¹ and is 82% of theoretical capacity, which is caused by HN-HC. Apparently, two voltage plateaus are observed at around 2.0 and 4.3 V during the second and third charge processes (Fig S7a), which could be assigned to the multi-step electrochemical reaction during this voltage range. Around 1.58 Na⁺ per formula unit can be reversibly extracted/inserted in the NFS/HN-HCNS-3 electrode. So the total reaction equations of NFS/HN-HCNS-3 electrode are as follows:



Furthermore, Fig S6a shows that the different electrodes all have lower energy efficiency due to the polarization over recharge, the lower intrinsic conductivity of NFS and the formation of the SEI layer. Keeping the charging potential at 4.65 V would likely cause many side reactions, such as structural rearrangement, electrolyte penetration, decomposition of electrolyte and oxidation of Fe ions [16]. The large fraction of the 'charging plateau' at 4.65 V would actually be due to the surface adsorption-desorption reactions in the mesoporous structure of HN-HC coating (Fig 1i), showing large capacitive contribution to the electrical energy storage (Fig 7). The polarization of all electrodes is significantly reduced and the capacity fading is smaller in the second cycle (Fig S6 b). In spite of a small fading in the second cycle caused by some side reactions, the discharge capacities of NFS/HN-HCNS-3 electrode perform a tendency toward stabilization in the following cycles (Fig S5ab). For NFS/HN-HCNS-3 electrode, 1.12 mol of Na⁺ was deintercalation during charging and

1.05 mol of Na^+ was intercalated during discharging. So the formation of the SEI layer consumed 0.07 mol of Na^+ .

Fig S7b shows rate performance of the NFS/HN-HCNS-3 hybrid electrode. The capacity attenuation is large between different rates. And the corresponding CV is shown in Fig S7c. Fig. 6g shows the long cycle stability performance of the NFS/HN-HCNS-3 hybrid electrode at 5 C, exhibiting a capacity of about 20.70 mAh g^{-1} after 750 cycles and corresponding to capacity retention of 56.8%. The Coulomb efficiency of the NFS/HN-HCNS-3 cathode is close to 100% during cycling, which means that the Na-ion insertion/extraction process is highly reversible. The cycle stability performance of the NFS/HN-HCNS-2 electrode at 5 C is shown in Fig. S5c. After 750 cycles, the capacity retention rate is only 26.6%. Obviously, the NFS/HN-HCNS-3 electrode has a higher capacity retention ratio than the NFS/HN-HCNS-2 electrode, which is mainly due to its unique carbon-coated framework structure, uniform nanoparticle size and excellent mesoporous structure.

In order to further study the electrochemical kinetics of Na^+ insertion and the energy storage mechanism, the CV curves of NFS/HN-HCNS-3 hybrid electrode at different scan rates in a voltage range of 1.5–4.6 V were tested, and the contribution ratios of capacitive at various sweep rates were calculated. Fig. 7a shows the nearly rectangular CV curves without distinct redox peaks, which is similar electrochemical behavior of electric double layer (EDL) capacitors and the characteristic of a surface-confined charge transfer process, verifying that NFS/HN-HCNS-3 also possessed EDL mechanism of surface-controlled processes [39,40]. The area of rectangular CV curves increases as increasing the scanning rate from 0.5 to 2.5 mV s^{-1} . Moreover, we calculate adjustable parameter b value from the logarithmic plot of the peak current versus sweep rate (Fig. 7b). The logarithmic relationship between peak current (i) and sweep rate (ν) can be described by equation (1) [41]:

$$i = av^b \quad (1)$$

$b=0.5$ represents the larger contribution from diffusion-controlled intercalation process of battery-type materials and $b=1.0$ means that the surface-controlled behavior of pseudocapacitive materials is the main one. The range of b values from 0.5 to 1.0 indicates a “transition” area between the surface control process of pseudocapacitive materials and the diffusion control process of battery-type materials, and the capacitive contribution increases with increasing b value [42]. The b -values of the cathodic and anodic peaks are 0.64 and 0.79 for the NFS/HN-HCNS-3 electrode, respectively (Fig. 7b), which indicates that the NFS/HN-HCNS-3 electrode has the higher capacitive contribution. The contribution ratio of surface-controlled behavior and diffusion controlled behavior can be calculated according to equation (2) [43].

$$i(v) = k_1 v + k_2 v^{1/2} \quad (2)$$

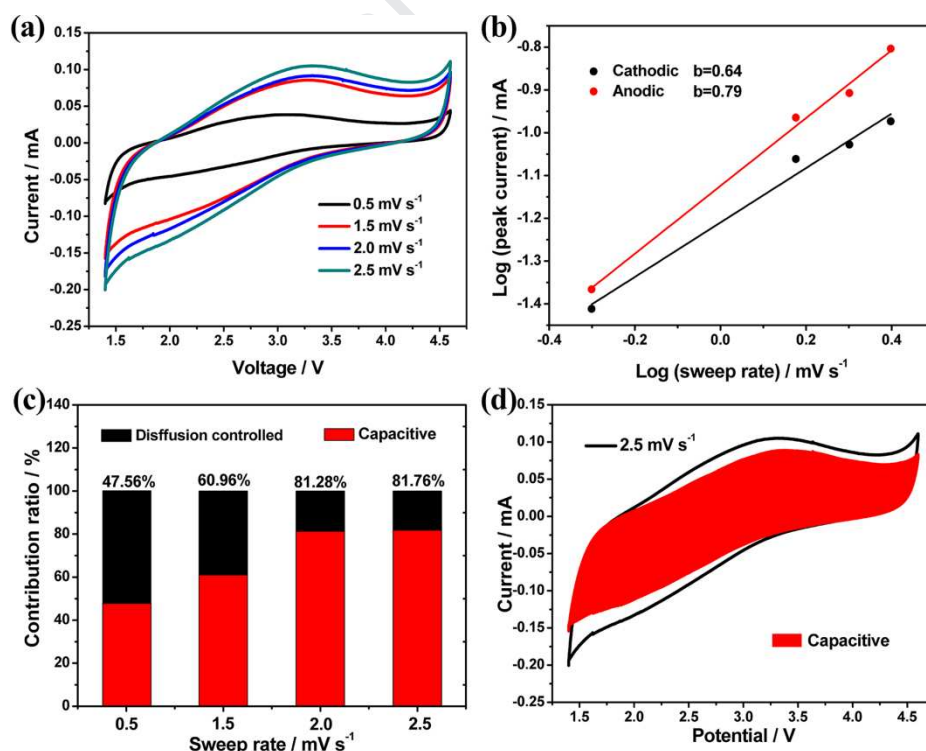


Fig. 7. (a) CV curves of NFS/HN-HCNS-3 hybrid electrode at various sweep rates. (b) Plots of log (sweep rate) versus log (peak current). (c) Contribution ratio of capacitive at various sweep rates. (d) Quantitative analysis of capacitive contribution at the sweep rate of 2.5 mV s⁻¹ in the CV curve.

Where k_1v is a capacitive contribution, and $k_2v^{1/2}$ is a contribution of the diffusion controlled process. The results show that the contribution ratio of the capacitive charge increases as the scan rate increases from 47.56% to 81.76% (Fig. 7c), indicating that its energy storage mechanism is a hybrid energy storage mechanism composed of the surface control process of supercapacitors and the diffusion control process of batteries. The contribution ratio of the capacitive charge is only 47.56% at the sweep rate of 0.5 mV s^{-1} , indicating that the contribution ratio of the capacitive reaction is low at lower sweep rates and the larger contribution is from the redox reactions of NFS. As shown in Fig. 7d, the contribution ratio of the capacitive charge is as high as 81.76% at the scan rate of 2.5 mV s^{-1} , indicating that the larger contribution is from the surface control process of mesoporous HN-HCNS coating. Hence, in the high sweep rate electrochemical test, the oxidation-reduction reactions of NFS are still in progress, but its contribution ratio is low.

Based on electrochemical analysis, we proposed a hybrid energy storage mechanism for the NFS/HN-HCNS-3 hybrid electrode. The interfaces between NFS layer and HN-HCNS layer not only generated extrinsic faradaic reactions by surface control process, but also provided a large accessible surface area for fast charge transfer and a shorter diffusion path for Na^+ insertion/extraction, thus significantly improving the power density. More importantly, NFS ultrathin sheet between two HN-HCNS layers can provide high Na ion storage interface and efficient electron/ion transport pathway for fast ion intercalation by diffusion control process and redox reactions, which also played an important role in enhancing the energy density and cycle life. Due to the collective and synergetic effect of different energy storage control processes, the NFS/HN-HCNS-3 with mesoporous carbon-coated structure utilizes the hybrid energy storage mechanisms and exhibits a high energy density and an excellent power density as well as high cycling stability.

Conclusion

In summary, with the purpose of low cost sodium-ion supercapacitors with high energy/power densities, high rate performance and long cycling stability, we have successfully synthesized a novel $\text{Na}_2\text{FeSiO}_4$ (NFS)/H-N-doped hard carbon nanosphere (HN-HCNS) hybrid electrode with mesoporous carbon-coated structure via a sol-gel method using ferrous gluconate as a template and carbon source. The several main synthesis conditions were optimized by using a multichannel battery testing system and EIS tests. The formation mechanism and hybrid energy storage mechanism of NFS/HN-HCNS hybrid electrode were investigated by using structural characterization techniques and cyclic voltammetry tests. The unique mesoporous carbon-coated structure provides high electrical conductivity, short ionic diffusion paths, large specific surface area and robust structural stability for NFS/HN-HCNS hybrid electrode. Due to the collective and synergetic effect of different energy storage control processes, the NFS/HN-HCNS-3 hybrid electrode with 7.98 wt% carbon exhibits a hybrid energy storage mechanism with high energy/power densities ($68.49 \text{ W h kg}^{-1}/2432 \text{ W kg}^{-1}$), excellent rate capability (the capacity retention rate of 56.8% at 5 C after the 750 cycles) and long cycling life (the capacity retention rate of 73.8% at 1 C after the 3300 cycles). This work can demonstrate that energy/power densities can be largely improved via the design of hybrid electrodes with a unique structure.

Author contributions

The manuscript was written through contributions of all authors. All authors have given approval to the final version of the manuscript.

Conflict of Interest

The authors declare no competing financial interest.

Appendix A. Supplementary data

Supplementary data associated with this article can be found in the online version at <http://>

AUTHOR INFORMATION

Corresponding Author

*Corresponding author. Tel: +86 18353108836.

E-mail address: hewen1960@126.com (W. He)

Acknowledgements

The authors thank National Natural Science Foundation of China (Grant No. 51672139, 51472127, 51272144) for the financial support.

References

- [1] S.-H. Xue, H. Xie, H. Ping, X.-M. Xu, Controlled synthesis of mesoporous nanostructured anatase TiO₂ on a genetically modified Escherichia coli surface for high reversible capacity and long-life lithium-ion batteries, *RSC Adv.* 6 (2016) 59422-59428. <https://doi.org/10.1039/C7SE00120G>.
- [2] V S. Ranganamy , S. Thayumanasundaram, J.-P. Locquet, Solvothermal synthesis and electrochemical properties of Na₂CoSiO₄ and Na₂CoSiO₄/carbon nanotube cathode materials for sodium-ion batteries, *Electrochim. Acta* 276 (2018) 102-110. <https://doi.org/10.1016/j.electacta.2018.04.166>.
- [3] Y.C. Liu, X.B. Liu, T.S. Wang, L.-Z. Fan, Research and application progress on key materials for sodium-ion batteries, *Sustain. Energ. Fuels.* 1 (2017) 986-1006. <https://doi.org/10.1039/C7SE00120G>.
- [4] D. Kundu, E. Talaie, V. Duffort, L.F. Nazar, The Emerging Chemistry of Sodium Ion Batteries for Electrochemical Energy Storage, *Angew. Chem. Int. Edit.* 54 (2015) 3431–3448. <https://doi.org/10.1002/anie.201410376>.
- [5] X.D. Xiang , K. Zhang, J. Chen, Recent Advances and Prospects of Cathode Materials for Sodium-Ion Batteries, *Adv. Mater.* 27 (2015) 5343-5364.

<https://doi.org/10.1002/adma.201501527>.

- [6] Y.J. Fang, Q. Liu, L.F. Xiao, X. Ai, High-Performance Olivine NaFePO_4 Microsphere Cathode Synthesized by Aqueous Electrochemical Displacement Method for Sodium Ion Batteries, *ACS Appl. Mater. Interfaces* 7 (2015) 17977-17984. <https://doi.org/10.1021/acsami.5b04691>.
- [7] Q.H. Zhang, X.D. Zhang, W. He, G.G. Xu, In situ fabrication of $\text{Na}_3\text{V}_2(\text{PO}_4)_3$ quantum dots in hard carbon nanosheets by using lignocelluloses for sodium ion batteries, *J. Mater. Sci. Technol.* 35 (2019) 2396-2403. <https://doi.org/10.1016/j.jmst.2019.06.002>.
- [8] N. Yabuuchi, K. Kubota, M. Dahbi, S. Komaba, Research Development on Sodium-Ion Batteries, *Chem. Rev.* 114 (2014) 11636-11682. <https://doi.org/10.1021/cr500192f>.
- [9] K. Kaliyappan, M.A. Jauhar, L. Yang, Z. Bai, Constructing a stable 3 V high-energy sodium ion capacitor using environmentally benign $\text{Na}_2\text{FeSiO}_4$ anode and activated carbon cathode, *Electrochim. Acta* 327 (2019) 134959. <https://doi.org/10.1016/j.electacta.2019.134959>.
- [10] S. Li, J. Guo, Z. Ye, X. Zhao, Zero-Strain $\text{Na}_2\text{FeSiO}_4$ as Novel Cathode Material for Sodium-Ion Batteries, *ACS Appl. Mater. Interfaces* 8 (2016) 17233-17238. <https://doi.org/10.1021/acsami.6b03969>.
- [11] Y.H. Kee, N. Dimov, A. Stayko, S. Okada, Investigation of metastable $\text{Na}_2\text{FeSiO}_4$ as a cathode material for Na-ion secondary battery, *Mater. Chem. Phys.* 171 (2016) 45-49. <https://doi.org/10.1016/j.matchemphys.2016.01.033>.
- [12] W. Guan, B. Pan, P. Zhou, J. Mi, A high capacity, good safety and low cost $\text{Na}_2\text{FeSiO}_4$ -based cathode for rechargeable sodium-ion battery, *ACS Appl. Mater. Interfaces.* 9 (2017) 22369-22377. <https://doi.org/10.1021/acsami.7b02385>.
- [13] X. Zhao, S. Wu, X. Lv, M.C. Nguyen, Exploration of tetrahedral structures in silicate cathodes using a motif-network scheme, *Sci. Rep-UK* 5 (2015) 15555. <https://doi.org/10.1038/srep15555>.
- [14] S. Yu, J.Q. Hu, M.B. Hussain, S.Q. Wu, Structural stabilities and electrochemistry of $\text{Na}_2\text{FeSiO}_4$ polymorphs: first-principles calculations, *J. Solid State Electr.* 22 (2018) 2237-2245. <https://doi.org/10.1007/s10008-018-3931-1>.
- [15] Z. Feng, M. Tang, Z. Yan, 3D conductive CNTs anchored with $\text{Na}_2\text{FeSiO}_4$ nanocrystals as a novel cathode material for electrochemical sodium storage, *Ceram. Int.* 44 (2018) 22019-22022. <https://doi.org/10.1016/j.ceramint.2018.08.186>.

- [16] B. Ali, A. Ur-Rehman, F. Ghafoor, M.I. Shahzad, Interconnected mesoporous $\text{Na}_2\text{FeSiO}_4$ nanospheres supported on carbon nanotubes as a highly stable and efficient cathode material for sodium-ion battery, *J. Power Sources* 396 (2018) 467-475. <https://doi.org/10.1016/j.jpowsour.2018.06.049>.
- [17] K. Kaliyappan, Z. Chen, Facile solid-state synthesis of eco-friendly sodium iron silicate with exceptional sodium storage behaviour, *Electrochimica Acta* 283 (2018) 1384-1389. <https://doi.org/10.1016/j.electacta.2018.07.034>.
- [18] M.S. Islam, R. Dominko, C. Masquelier, C. Sirisopanaporn, Silicate Cathodes for Lithium Batteries: Alternatives to Phosphates? *J. Mater. Chem.* 21 (2011) 9811-9818. <https://doi.org/10.1039/C1JM10312A>.
- [19] L. Kang, Z. Yang, Y. Xu, W. Jiang, Self-assembly of Fe_2O_3 /ordered mesoporous carbons for high-performance lithium-ion batteries, *J. Electroanal. Chem.* 817 (2018) 65-72. <https://doi.org/10.1016/j.jelechem.2018.03.066>.
- [20] L. Yang, W. Liu, H. Wang, S. Liu, A low-cost and one-step synthesis of a novel hierarchically porous $\text{Fe}_3\text{O}_4/\text{C}$ composite with exceptional porosity and superior Li^+ storage performance, *RSC Adv.* 5 (2015) 102993-102999. <https://doi.org/10.1039/c5ra24166a>.
- [21] L. Wang, C. Yang, S. Dou, S. Wang, Nitrogen-doped hierarchically porous carbon networks: synthesis and applications in lithium-ion battery, sodium-ion battery and zinc-air battery, *Electrochim. Acta* 219 (2016) 592-603. <https://doi.org/10.1016/j.electacta.2016.10.050>.
- [22] Z. Yan, W. He, X. Zhang, X. Yang, N-doped hard carbon ultrathin film-coated Fe_{1-x}S nanoparticles with multi-morphologies for cheap Li ion battery anodes, *J. Mater. Sci.-Mater. Electron.* 30 (2019) 4527-4540. <https://doi.org/10.1007/s10854-019-00742-1>.
- [23] Z. Wang, C. Yang, T. Lin, H. Yin, H \square Doped Black Titania with Very High Solar Absorption and Excellent Photocatalysis Enhanced by Localized Surface Plasmon Resonance, *Adv. Funct. Mater.* 23 (2013) 5444-5450. <https://doi.org/10.1002/adfm.201300486>.
- [24] Z. Ye, X. Zhao, S. Li, S. Wu, Robust diamond-like Fe-Si network in the zero-strain $\text{Na}_x\text{FeSiO}_4$ cathode, *Electrochim. Acta* 212 (2016) 934-940. <https://doi.org/10.1016/j.electacta.2016.07.073>.
- [25] P Wu, S.Q. Wu, X. Lv, X. Zhao, Fe-Si networks in $\text{Na}_2\text{FeSiO}_4$ cathode materials, *Phys. Chem. Chem. Phys.* 18 (2016) 23916-23922. <https://doi.org/10.1039/c6cp05135a>.

- [26] B Chang, Y Guo, Y Li, H. Yin, Graphitized hierarchical porous carbon nanospheres: simultaneous activation/graphitization and superior supercapacitance performance, *J. Mater. Chem. A* 3 (2015) 9565-9577. <https://doi.org/10.1039/c5ta00867k>.
- [27] Z. Zheng, Y. Wang, A. Zhang, T. Zhang, Porous $\text{Li}_2\text{FeSiO}_4/\text{C}$ nanocomposite as the cathode material of lithium-ion batteries, *J. Power Sources* 198 (2012) 229-235. <https://doi.org/10.1016/j.jpowsour.2011.09.066>.
- [28] S. Zhang, C. Deng, F.L. Liu, Q. Wu, Impacts of in situ carbon coating on the structural, morphological and electrochemical characteristics of $\text{Li}_2\text{MnSiO}_4$ prepared by a citric acid assisted sol-gel method, *J. Electroanal. Chem.* 689 (2013) 88-95. <https://doi.org/10.1016/j.jelechem.2012.11.028>.
- [29] H. Gao, L. Wang, Y. Zhang, A. Zhang, Tartaric acid assisted synthesis of $\text{Li}_2\text{FeSiO}_4/\text{C}$: Effect of carbon content on the electrochemical performance of $\text{Li}_2\text{FeSiO}_4/\text{C}$ for lithium ion batteries, *Powder Technol.* 253 (2014) 638-643. <https://doi.org/10.1016/j.powtec.2013.12.034>.
- [30] A.C. Ferrari, J. Robertson, Interpretation of Raman spectra of disordered and amorphous carbon, *Phys. Rev. B* 61 (2000) 14095-14107. <https://doi.org/10.1103/PhysRevB.61.14095>.
- [31] L. Chen, Y. Zhao, S. Liu, L. Zhao, Hard Carbon Wrapped $\text{Na}_3\text{V}_2(\text{PO}_4)_3/\text{C}$ Porous Composite Extending Cycling Lifespan for Sodium-Ion Batteries, *ACS Appl. Mater. Interfaces* 9 (2017) 44485-44493. <https://doi.org/10.1021/acsami.7b14006>.
- [32] Z. Zhou, Y. Shao, X. Gao, Z. Liu, Structural regulation of polypyrrole nanospheres guided by hydrophobic chain length of surfactants, *J. Mater. Sci.* 54 (2019) 14309-14319. <https://doi.org/10.1007/s10853-019-03897-8>.
- [33] Z. Xiu, M.H. Alfaruqi, J. Gim, J. Song, MOF-derived mesoporous anatase TiO_2 as anode material for lithium-ion batteries with high rate capability and long cycle stability, *J. Alloy Compd.* 674 (2016) 174-178. <https://doi.org/10.1016/j.jallcom.2016.02.238>.
- [34] B.D. Mofrad, M. Rezaei, M. Hayati-Ashtiani, Preparation and characterization of Ni catalysts supported on pillared nanoporous bentonite powders for dry reforming reaction, *Int. J. Hydrogen Energ.* 44 (2019) 27429-27444. <https://doi.org/10.1016/j.ijhydene.2019.08.194>.

- [35] B. Heidrich, A. Heckmann, K. Beltrop, M. Winter, Unravelling charge/discharge and capacity fading mechanisms in dual-graphite battery cells using an electron inventory model, *Energy Storage Mater.* 21 (2019) 414-426. <https://doi.org/10.1016/j.ensm.2019.05.031>.
- [36] H.F. Xiang, X. Zhang, Q.Y. Jin, C.P. Zhang, Effect of capacity matchup in the $\text{LiNi}_{0.5}\text{Mn}_{1.5}\text{O}_4/\text{Li}_4\text{Ti}_5\text{O}_{12}$ cells, *J. Power Sources* 183 (2008) 355-360. <https://doi.org/10.1016/j.jpowsour.2008.04.091>.
- [37] Y. Yan, B. Ren, Y. Xu, J. Wang, Preparation and Electrochemical Properties of Coral-like $\text{Li}_2\text{FeSiO}_4/\text{C}$ Cathode Material by Two-Step Precipitation Method, *J. Electron. Mater.* 45 (2016) 4943-4951. <https://doi.org/10.1007/s11664-016-4676-1>.
- [38] Q. Pan, L. Qin, J. Liu, H. Wang, Flower-like ZnO-NiO-C films with high reversible capacity and rate capability for lithium-ion batteries, *Electrochim. Acta.* 55 (2010) 5780-5785. <https://doi.org/10.1016/j.electacta.2010.05.017>.
- [39] C. Lian, K. Liu, K.L. Van Aken, Y. Gogotsi, Enhancing the Capacitive Performance of Electric Double-Layer Capacitors with Ionic Liquid Mixtures, *ACS Energy Lett.* 1 (2016) 21-26. <https://doi.org/10.1021/acsenergylett.6b00010>.
- [40] H. Yang, J. Yang, Z. Bo, X. Chen, Kinetic-Dominated Charging Mechanism within Representative Aqueous Electrolyte-based Electric Double-Layer Capacitors, *Phys. Chem. Lett.* 8 (2017) 3703-3710. <https://doi.org/10.1021/acs.jpcllett.7b01525>.
- [41] K.V. Sankar, R.K. Selvan, The ternary $\text{MnFe}_2\text{O}_4/\text{graphene}/\text{polyaniline}$ hybrid composite as negative electrode for supercapacitors, *J. Power Sources* 275 (2015) 399-407. <https://doi.org/10.1016/j.jpowsour.2014.10.183>.
- [42] X. Yang, R.Y. Zhang, J. Zhao, Z.X. Wei, Amorphous Tin-Based Composite Oxide: A High-Rate and Ultralong-Life Sodium-Ion-Storage Material, *Adv. Energy Mater.* 8 (2017) 1701827. <https://doi.org/10.1002/aenm.201701827>.
- [43] J. Pan, S. Chen, D. Zhang, X. Xu, SnP_2O_7 Covered Carbon Nanosheets as a Long-Life and High-Rate Anode Material for Sodium-Ion Batteries, *Adv. Funct. Mater.* 28 (2018) 1804672. <https://doi.org/10.1002/adfm.201804672>.

Highlights

- ▶ $\text{Na}_2\text{FeSiO}_4/\text{H-N}$ -doped mesoporous hard carbon nanosphere hybrid cathodes was synthesized.
- ▶ Ferrous gluconate template controlled the formation of mesoporous carbon-coated structure.
- ▶ This structure gives a remarkable synergic effect of Na-ion battery-supercapacitor.
- ▶ This hybrid electrode delivers high energy and power densities.

Declaration of interests

The authors declare that they have no known competing financial interests or personal relationships that could have appeared to influence the work reported in this paper.

The authors declare the following financial interests/personal relationships which may be considered as potential competing interests:

Journal Pre-proof